Whole-body three-dimensional optoacoustic tomography system for small animals

Hans-Peter Brecht
Richard Su
Fairway Medical Technologies, Inc.
9431 West Sam Houston Parkway South
Houston, Texas 77099
E-mail: aoraevsky@fairwaymed.com

Matthew Fronheiser
Seno Medical Instruments, Inc.
3838 Medical Drive
San Antonio, Texas 78230

Sergey A. Ermilov
Andre Conjusteau
Alexander A. Oraevsky
Fairway Medical Technologies, Inc.
9431 West Sam Houston Parkway South
Houston, Texas 77099

Abstract. We develop a system for three-dimensional whole-body optoacoustic tomography of small animals for applications in preclinical research. The tomographic images are obtained while the objects of study (phantoms or mice) are rotated within a sphere outlined by a concave arc-shaped array of 64 piezocomposite transducers. Two pulsed lasers operating in the near-IR spectral range (755 and 1064 nm) with an average pulsed energy of about 100 mJ, a repetition rate of 10 Hz, and a pulse duration of 15 to 75 ns are used as optical illumination sources. During the scan, the mouse is illuminated orthogonally to the array with two wide beams of light from a bifurcated fiber bundle. The system is capable of generating images of individual organs and blood vessels through the entire body of a mouse with spatial resolution of ~0.5 mm. [DOI: 10.1117/1.3259361]

Keywords: small animal imaging; optoacoustic; image reconstruction; functional imaging; blood; vasculature.

Paper 09175PR received May 19, 2009; revised manuscript received Aug. 21, 2009; accepted for publication Sep. 10, 2009; published online Nov. 18, 2009. This paper is a revision of a paper presented at the SPIE conference on Photons Plus Ultrasound: Imaging and Sensing 2009, January 2009, San Jose, California. The paper presented there appears (unrefereed) in SPIE Proceedings Vol. 7177.

1 Introduction

Small animals, especially mice, are extensively used as a mammalian model for human disease in preclinical research. The variety of imaging techniques used for small animals include high-frequency ultrasound,[1,2] micro-computed tomography[3] (micro-CT), micro magnetic resonance imaging[4] (micro-MRI), and nuclear medicine techniques[5] that can be used for tracking of the disease or monitoring of treatment in the animals. Additionally, optical imaging techniques such as bioluminescence imaging,[6] fluorescence imaging,[7] or diffusion optical tomography[8] are being used for the characterization of tissue or detection of molecular probes.[9] These all-optical imaging techniques show limited resolution at depths beyond a few millimeters due to the strong optical scattering in opaque biological tissue. Optoacoustic imaging significantly improves the spatial resolution of the optical images by converting the diffuse light that is absorbed in tissue into ultrasound. Scattering and attenuation of ultrasound in the frequency range below 10 MHz is minor in tissue compared with the scattering and attenuation of light. Therefore, optoacoustic imaging that combines the spectral sensitivity and contrast of optical imaging with the spatial resolution of acoustic imaging has the advantage of providing high contrast and high resolution simultaneously.[10]

The high optical contrast between the hemoglobin of blood and the surrounding tissue makes optoacoustic imaging an optimally suited technology for visualization of blood vessels and blood distribution in organs.[11–13] Maslov et al.[14] and Wang et al.[15] have been instrumental in developing an optoacoustic microscope system to image blood vessels in the mouse. Zhang et al. have developed a high-resolution 3-D scanning imaging system based on optical interferometry.[16] Since aggressively growing tumors are densely vascularized, optoacoustic systems have been used in the past to image various tumors on the macroscopic and microscopic scales.[17–23] In cancer research using orthotopic models, in which primary tumors are induced in the internal organs and their metastases spontaneously appear in various parts of the animal body, whole-body imaging is desirable. Whole-body mouse imaging may enable the detection of tumors in internal organs, not only subcutaneous tumors. Kruger et al. successfully developed the first 2-D imaging system and imaged a sacrificed mouse using a commercial linear ultrasound array and rotation motor to generate an optoacoustic slices.[24] As the next-generation device, using the concept of an arc-shaped array previously developed for breast imaging,[25] the same group developed a 3-D system for imaging the whole mouse body.[26] The system showed good spatial resolution and was used to image optical dye phantoms, kidneys, and major vasculature of two sacrificed mice. However, *in vivo* imaging was not enabled and the need for the whole-body 3-D optoacoustic tomography in small animals still exists. The major merit of optoacoustic tomography is that in addition to high-contrast visualization of the animal anatomy, it can provide functional information such as blood concentration and its level of oxygenation[22,27] and molecular information based on spectroscopy and exogenous contrast agents.[28–31] We developed an

Address all correspondence to: Alexander Oraevsky, Fairway Medical Technologies, Inc. 9431 West Sam Houston Parkway South, Houston, Texas 77099. Tel; 713-772-7867; Fax: 713-772-2010; E-mail: aoraevsky@fairwaymed.com

1083-3668/2009/14(6)/064007/8/$25.00 © 2009 SPIE

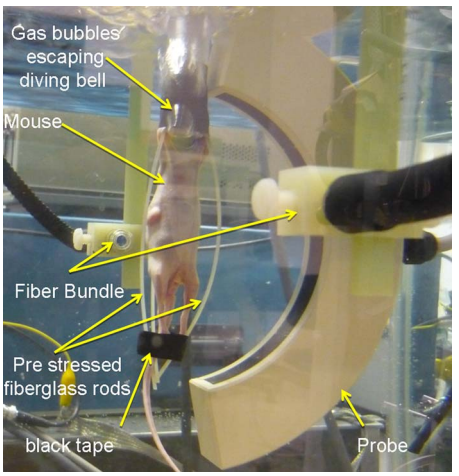

Fig. 1 Picture of a mouse during a scan, showing the placement of the mouse and illumination with respect to the array of wideband ultrasonic transducers.

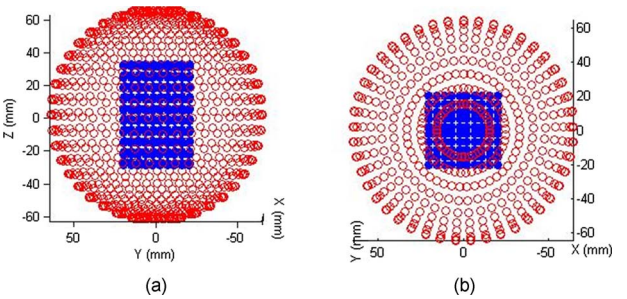

Fig. 2 (a) Side view and (b) top view of the reconstruction sphere showing the geometric representation of the detector placement during one full rotation of the mouse. The blue area represents the location of the mouse. The blue area represents the location of the mouse. The detector density is higher at the poles in comparison to the equator. (Color online only.)

optoacoustic system for 3-D tomography of the whole mouse body and tested its performance in phantoms and live mice.[32] A detailed description of the system technical parameters in this paper is followed by a discussion of its potential utility in preclinical research.

2 Materials and Methods

2.1 *System Description*

The optoacoustic mouse imaging system consists of four main components: fiber-optic light delivery, a mouse holder with translation and rotation, an array of transducers (detectors), and data acquisition and imaging electronics. We used the following two sources of optical illumination: (1) an alexandrite laser (Ta-2, Light Age, Inc., Somerset, New Jersey), operating at a 755-nm wavelength, a 10-Hz pulse repetition rate, energy of ~100 mJ per pulse, and a pulse duration of ~75 ns; and (2) Nd:YAG laser (Brilliant, Quantel, Bozeman, Montana), operating at a 1064-nm wavelength, a 10-Hz pulse repetition rate, ~100 mJ of energy per pulse, and pulse duration of ~15 ns. Light delivery was performed orthogonally to the array of acoustic transducers by a bifurcated, randomized fiber bundle (Schott AG, Germany) of 48 in. in length. The diameter on the input side was 0.4 in., while the diameter on the bifurcated output side was 0.25 in.. Transmission loss within the fiber bundle was about 50%. After leaving the fiber, the two light beams, $E=25$ mJ each, were expanded to a diameter of 8 cm at the target. Figure 1 shows a mouse in the tank during the scan.

Imaging was performed in a water tank with dimensions of 20 in. L × 16 in. W × 17 in. H. The temperature in the water tank was maintained at 36 °C by heating elements placed underneath. These heat pads were controlled by a proportional-integral-derivative controller (PID temperature controller) (Watlow Inc., Columbia, Missouri) with a precision of 0.1 °C. The tight control of the temperature ensured a stable speed of sound in the water surrounding mouse, which is necessary for accurate reconstruction of the 3-D mouse volumes. The rotation of the mouse was performed by a dc motor with an optical encoder (Faulhaber Gmbh, Schoenaich, Germany), while the position of the array was controlled by three motorized linear stages (IAI Inc., Torrance, California).

The optoacoustic signals were acquired with a 64-element arc-shaped piezocomposite array designed in our lab and custom built by Imasonic, SAS (France). The center frequency of ultrasonic transducers was 3.1 MHz, and the bandwidth was ⩾80% at the −6-dB point. The piezocomposite elements had square dimension of 2 mm and were spaced 0.7 mm apart. The focal length of the array was 65 mm and the overall angular aperture between element 1 and 64 was 152 deg, which gave an angle of 2.4 deg between elements. The step size for the rotation was set to 2.4 deg to ensure even detector spacing in the equatorial and meridianal directions. The data acquisition system consisted of three custom-designed 48 channel analog amplifiers featuring an input impedance of 750 kΩ, a variable gain between 0 and 70 dB, a bandwidth of 25 kHz to 13 MHz at the −3-dB point, and an input noise of 2 nV/$\sqrt{\text{Hz}}$. For the mouse scan, the amplifiers were set to 60-dB amplification. Data digitalization was performed with two in-house-designed 32-channel boards containing analog-to-digital converters with a sampling rate of up to 40 MHz, a field programmable gate array (Stratix FPGA, Altera (San Jose, California) for signal processing and data transfer to a personal computer through the Ethernet protocol. A standard personal computer (Intel/Pentium IV, 3 GHz) running our custom-made LOIS software was used to capture the data and reconstruct optoacoustic images.

2.2 *Signal Processing and Image Reconstruction*

Multiple data acquisitions with the mouse rotating about the central axis of the arc-shaped acoustic array are equivalent to a single acquisition with acoustic transducers distributed over the corresponding spherical surface (see Fig. 2). In our studies, a full circle (360-deg) rotation was performed with 150 steps of 2.4 deg for each step, thus representing data acquisition with 9600 virtual transducers placed on the reconstruction sphere with an animal enclosed in its center [Fig. 2(a)]. The captured optoacoustic signals were filtered before undergoing reconstruction. We routinely used a second-order Butterworth filter with a bandpass between 250 kHz and 5 MHz. This filter worked best for processing of optoacoustic signals

in preparation for reconstruction of mouse organs and major blood vessels. A more sophisticated signal filtering was required for visualization of smaller vasculature or a combination of larger and smaller tissue structures presented on the same image. For this purpose, we used previously developed multiscale wavelet filter based on a wavelet resembling typical N-shaped optoacoustic signals.[33] Later we optimized this wavelet to replicate the third derivative of the Gaussian wavelet, which can be used to enhance sharpness of the boundaries while significantly reducing low-frequency acoustic trends for optoacoustic sources of arbitrary shapes.[34] Nine scales of this wavelet covering a wide range of frequencies from 4 to 1024 digital samples enabled flexibility in the complex signal processing. An advantage inherent in the multiscale wavelet processing is that the wavelet filter simultaneously serves as an integrator, resulting in conversion of bipolar optoacoustic pressure profiles into monopolar profiles of the absorbed optical energy.[35]

Three-dimensional tomographic reconstruction was performed using a 3-D reconstruction-algorithm-based radial back projection of filtered and simultaneously integrated optoacoustic signals,[25] where the integration was achieved through a multiscale wavelet transform.[32] Such reconstruction in the 3-D case uses the complete data set and, therefore, is rigorous. Since rotation of an arc of transducers around a vertical axis generates a variable density of the detector elements continuously increasing toward the poles of the reconstruction sphere, we normalized the optoacoustic signals by the local transducer density employing a weighting factor of A, which compensated for distortions caused by the transducer density [Fig. 2(b)]:

$$\overline{S_t} = \frac{2\pi r^2 \sin\varphi \cdot \Delta\varphi}{N_{\text{angles}}} S_i = C \sin\varphi S_i, \qquad (1)$$

where $\overline{S_t}$ is the normalized optoacoustic signal used in the reconstruction, S_t is the originally measured optoacoustic signal, r is the radius of the acoustic array, φ is the zenith angle in the spherical coordinate system associated with the reconstruction sphere (Fig. 2), $\Delta\varphi$ is the elevation step between transducers in the acoustic array, and N_{angles} is the number of mouse rotation steps. The parameter C, which incorporates the geometry of the array and the precision of the mouse rotation, is constant for every transducer on the reconstruction sphere.

2.3 *Postprocessing of Tomographic Images*

A commercial 3-D image visualization package, VolView-2.0 (Kitware, Clifton Park, New York), was used for the image postprocessing. We designed a postprocessing routine for the 3-D optoacoustic image based on the assumption that the majority of the voxel data is comprised of noise, situated around the principal mode of the distribution of the image intensity. The principal mode was determined from the maximum of the voxel brightness histogram. For voxels with values less than this mode, the opacity was set to 0. Of the remaining voxel values, the bottom 60% of values were made transparent to limit noise from being displayed. This kind of manipulation can be done in the setting of the Scalar Opacity Map of Volview. A 0.5 intensity value was placed in the Scalar Opacity Map at the 90% mark, and an intensity value of 1 was placed at the 100% mark to make the relevant voxels brighter and more easily seen. The opacity of the remaining data was allowed to linearly increase toward these marks of the intensity histogram.

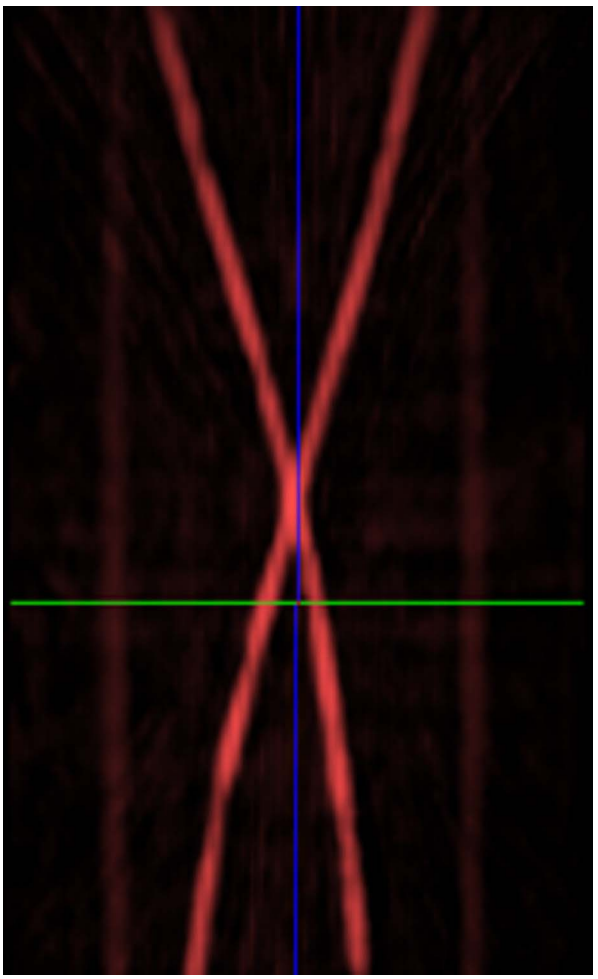

Fig. 3 Reconstructed optoacoustic volume of a hair cross made from 200-μm-diam horse hair at a 26-deg angle used for resolution studies.

The image palette was set to gray scale for those values with nonzero opacity according to the following algorithm. The brightness value of 0, i.e., black color, was set to the values that were most proximal to the intensity histogram mode. The next 70% of the data with nonzero opacity was linearly scaled between 0 and 0.5 color values. The brightness value of 1, i.e., white color, was assigned to the most opaque 10% of the data, with the remaining data linearly scaled between 0.5 and 1 color values in the order of increasing opacity. We also applied the Strong Edge Detection processing available in Volview, which can be found in the Gradient Opacity Mapping, to emphasize large intensity changes between neighboring voxels. The gradient opacity mapping assigns an opacity multiplier to the gradient magnitudes. It calculates the difference in intensity between the voxels in all three dimensions and generates a gradient intensity histogram. This enables clearing the regions with similar voxel intensities, and enhances the areas of sharp intensity change, effectively performing 3-D edge detection during rendering.

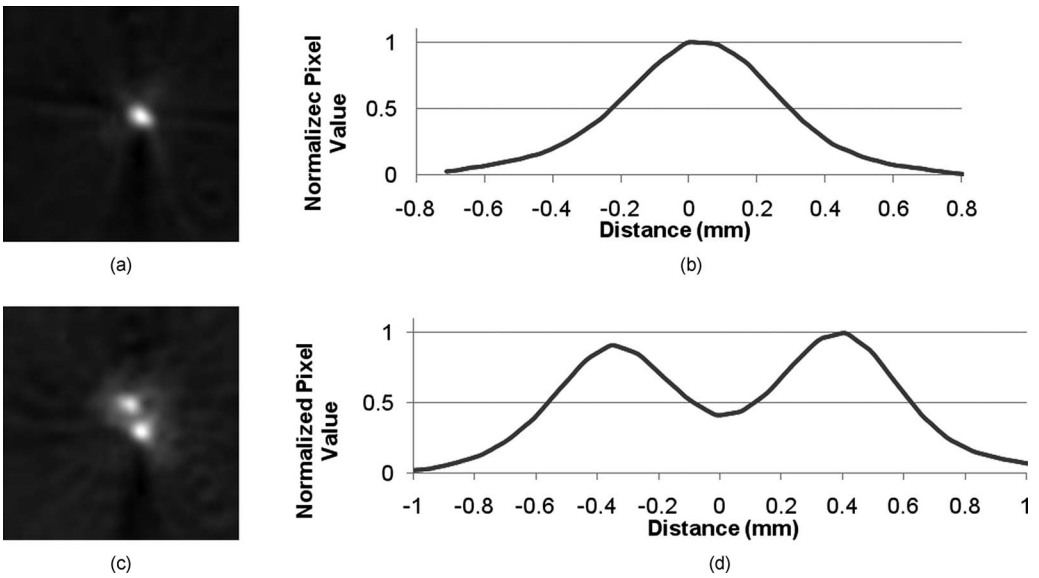

Fig. 4 (a) Vertical slice of the hair cross at the location of the intersection of the two horse hairs, (b) normalized intensity profile through the maximum of the *x-y* slice, (c) vertical slice of the hair cross 1.7 mm below the location of the intersection of the two horse hairs, (d) normalized intensity profile through the two maxima of the *x-y* slice. The normalized intensity value drops to 50% of the maxima at a separation of ~0.5 mm between the two maxima.

2.4 *Mouse Holder*

All procedures of the mouse study were in compliance with our Institutional Animal Use and Care Committee (IACUC) protocol. The mouse was anesthetized with isoflurane in pure oxygen using an isoflurane distribution unit (Summit Anesthesia Solutions, Bend, Oregon) and then placed into a custom-made mouse holder consisting of two main parts (see Fig. 1). The top part is a hollow cylinder with one end drilled in a conical manner so as to be able to fit the mouse's nose and face. The bottom part consisted of an acrylic disk with a center hole for the tail to pass through. The top and bottom part of the mouse holder were connected with pretensioned fiber glass rods. The mouse was held in place with tape. The mouse's arms were attached on the outside of the top part of the mouse holder and the legs of the mouse were attached to the disk at the bottom of the mouse holder so as to minimize shifts and movements from the mouse rotation. The soft tape ensured that the mouse was held in place with minimal pressure so as not to restrict blood flow into the extremities. The anesthesia gas was delivered to the mouse holder via a central freely rotating shaft inserted into the upper cylindrical part of the mouse holder. The upper portion of the mouse holder's conical opening created a "diving bell" for the head of the mouse with the anesthesia gas pumped into it and enabled the mouse to breathe freely while placed in the tank under water with excess gas bubbling into the tank. The breathing cone simultaneously shielded the eyes of the mouse from the laser exposure. The flow rate of oxygen was 2 L/min with an isoflurane concentration of 2% for initial anesthesia. Isoflurane concentration was later varied between 1 and 2% on continuous inspection of the animal. Euthanasia was performed after the experiment through spinal dislocation under 5% isoflurane in oxygen.

3 Results

3.1 *Resolution of the Optoacoustic Array*

The resolution of the imaging system was determined using a cross made from two horse hairs. The thickness of the hairs was 200 μm. The two hairs placed at an angle of 20 deg between them. After placement in the tank, the hair cross was illuminated orthogonally to the acoustic array with the dual fiber bundle and the data were collected. A 3-D volume was reconstructed with a voxel size of 0.1 mm. Figure 3 shows the optoacoustic image of the hair cross. Two horizontal slices orthogonal to the image depicted in Fig. 3 were selected from the volume and are presented in Figs. 4(a) and 4(c). The first slice [Fig. 5(a)] was at the location of the intersection of the

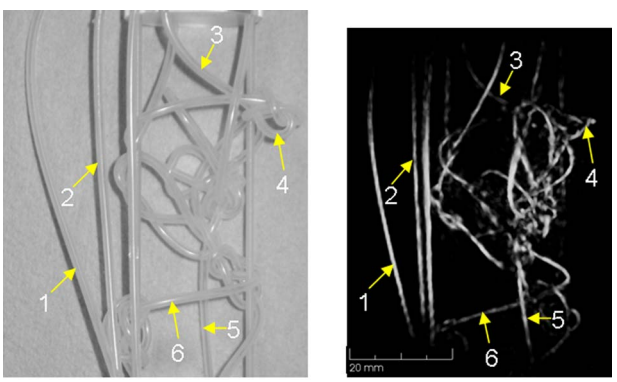

Fig. 5 (a) Photograph of the 0.75-mm-inner-diameter silicone tube maze used as a phantom to simulate blood vessels and (b) optoacoustic volumetric image of silicone tubes filled with $CuSO_4$ solution adjusted to an absorption coefficient of 9 cm^{-1}.

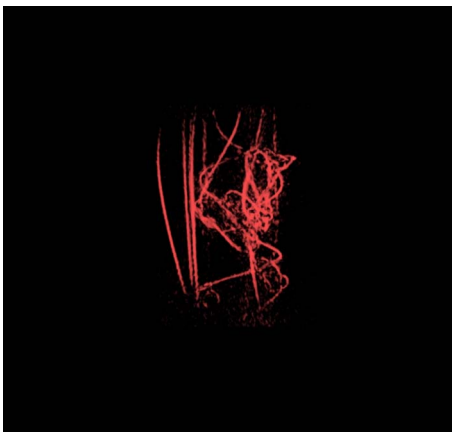

Video 1 This video corresponds to Fig. 5, showing a 3-D optoacoustic volumetric image of silicone tubes filled with $CuSO_4$ solution adjusted to an absorption coefficient of 9 cm^{-1} (QuickTime, 3.8 MEG). [URL: http://dx.doi.org/10.1117/1.3259361.1].

hair cross where the area of the pixel intensity is the smallest. Figure 4(b) shows the normalized intensity profile through the center of the hair cross. The thickness of the hair cross is ~0.5 mm at full width at half maximum (FWHM). Taking the width of the hair into account we get ~0.3-mm resolution, which corresponds to a frequency of 4.5 MHz, well within the ultrasonic frequency band of the probe. Subsequent slices were analyzed below the hair intersection. We determined a slice where the intensity between the two maxima decreased to 50% of the values of the maxima. An image of this second slice is shown in Fig. 4(c). The distance between the two maxima was ~0.8 mm [Fig. 4(d)]. This shows that after subtraction of the width of the hairs the resolvable distance between two points is 0.6 mm.

3.2 *Phantoms Used in Studies of Optoacoustic Image Contrast and Resolution*

For the phantom studies, a cupric sulfate solution with an absorption coefficient of 9 cm^{-1} contained in 0.75-mm internal-diam silicone tubing was used to simulate blood vessels. The tubes were wrapped and entangled within a holder made from acrylic plates and fiberglass rods. Fiberglass is a glass-cloth laminate with an epoxy resin binder (Professional Plastics, Fullerton, California). In our test, it showed excellent strength, no water absorption, and minimal optoacoustic signals were generated by the material. Figure 5(a) shows a picture of the tube setup used in the phantom studies, while Fig. 5(b) shows a projection of the optoacoustic volume (also see Video 1). Visual comparisons show good agreement between the photograph and reconstructed volume, indicating the ability to image and visualize complex structures with sufficient clarity, a requirement for whole body mouse imaging.

3.3 *Mouse Images*

Figure 6 shows the optoacoustic volume of a mouse with the alexandrite laser at 755 nm and a vertically elongated oval beam (also see Video 2). The Gaussian output beam from the fiber bundle was elongated with cylindrical lenses into an oval beam shape to facilitate a more uniform illumination over the mouse body. This allowed the imaging of a larger section of

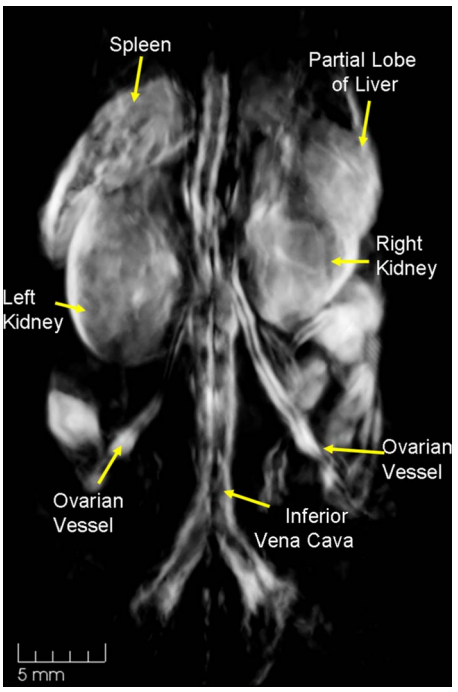

Fig. 6 Three-dimensional optoacoustic volume of a nude mouse illuminated at 755 nm with optical fluence of 1 mJ/cm^2, showing an area of the mouse with bifurcation of the inferior vena cava extended into the gonadal (ovarian) veins. Both kidneys are visualized as well as the spleen and a partial lobe of the liver.

the mouse, resulting in the visualization of the abdominal aorta and its bifurcation into the femoral veins. Additionally, both kidneys are visualized as well as the spleen and a partial lobe of the liver. The imaged mouse was female and the ovarian vessels were visible.

The results from a male mouse scan are shown in Fig. 7 (also see Video 3). This mouse was also illuminated with the alexandrite laser (755 nm), and similarly to Fig. 6, it shows

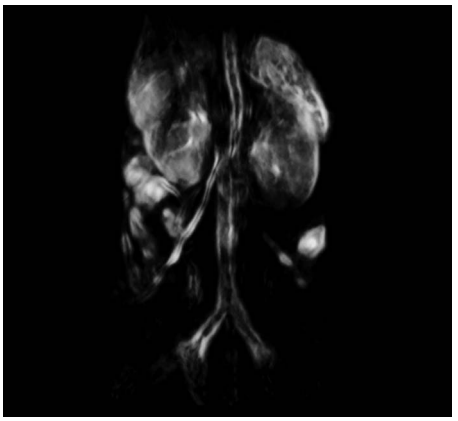

Video 2 This video corresponds to Fig. 6, showing a 3-D optoacoustic volume of a nude mouse illuminated at 755 nm with optical fluence of 1 mJ/cm^2. The rotating image shows an area of the mouse with bifurcation of the inferior vena cava extended into the gonadal (ovarian) veins. Both kidneys are visualized as well as the spleen and a partial lobe of the liver (QuickTime, 2 MEG). [URL: http://dx.doi.org/10.1117/1.3259361.2].

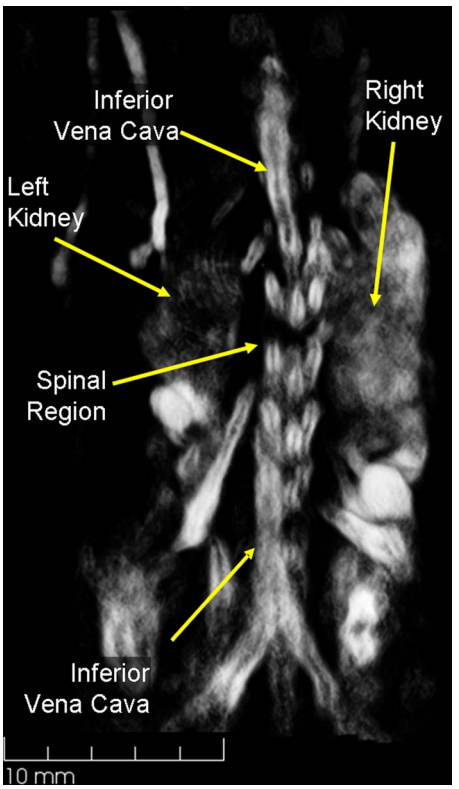

Fig. 7 Optoacoustic volume of a nude mouse illuminated at 755 nm with optical fluence of 1 mJ/cm^2 clearly showing the spine (contrast of the spine is provided by spinal microvasculature), the descending inferior vena cava, and its bifurcation into external and internal femoral veins, and a view of the left and right kidneys.

the descending aorta with bifurcation. These features of mouse anatomy are similar in both images (Figs. 6 and 7), indicating that key features are reproducible in different subjects. However, only an obscured view of the kidneys is displayed in Fig. 7. On the other hand, Fig. 7 clearly shows the spine of the mouse. The image formation in the spinal region could be from the network of small and unresolved blood vessels supplying the vertebra. While the spine is visible in most mouse volumes it was especially clear in this volume, because the mouse was located in the holder in a way that placed the mouse spine at the center of rotation where the sensitivity and resolution of the probe is the highest.

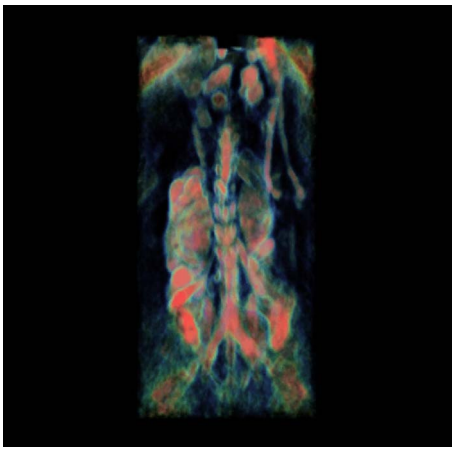

Video 3 This video corresponds to Fig. 7, showing an optoacoustic volume of a nude mouse illuminated at 755 nm with optical fluence of 1 mJ/cm^2 clearly showing the spine (contrast of the spine is provided by spinal microvasculature), the descending inferior vena cava, and its bifurcation into external and internal femoral veins, and a view of the left and right kidneys (QuickTime, 2 MEG).
[URL: http://dx.doi.org/10.1117/1.3259361.3].

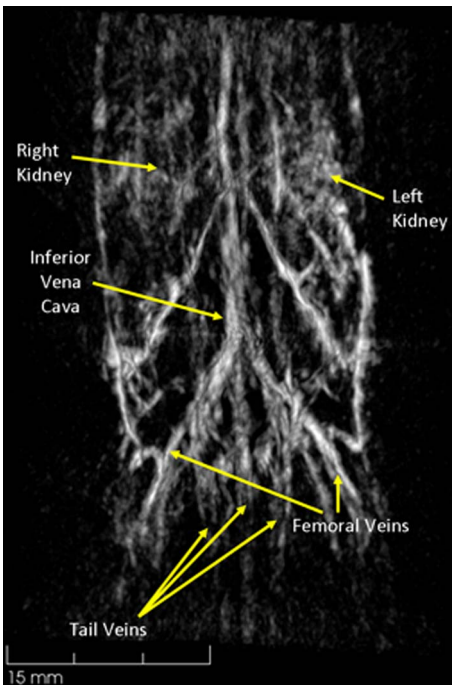

Fig. 8 Optoacoustic volume of a nude mouse illuminated at 1064 nm, at optical fluence of 1 mJ/cm^2, showing the mouse body vasculature including descending inferior vena cava and its bifurcation into the external and internal femoral veins and the three tail veins. Additionally, there is a partial view of the left and right kidney vasculature.

The optoacoustic volume from another mouse scan (Fig. 8) was performed using the Nd:YAG laser at 1064 nm (also see Video 4). It shows the descending aorta, the abdominal aorta, and its bifurcation into the femoral veins. Additionally, the three veins in the tail were imaged. The left and right kidneys are fainter than comparable images performed with an illumination of 755 nm. Blood in the mouse vasculature was highly oxygenated due to the use of 50% oxygen along with anesthesia. Therefore, laser illumination at 1064 nm, which is strongly absorbed by oxygenated blood, revealed both arterial and venous vasculature, while emphasizing veins due to their larger diameters.

4 Discussion

A whole-body optoacoustic mouse imaging system was successfully developed. The anatomical features correlated well with published mouse anatomy.[36] The current setup is capable of imaging organs and blood vessels. To detect microvasculature and the angiogenesis network of tumors the resolution of the imaging system must be improved. Despite being expanded along a mouse body, the Gaussian light distribution

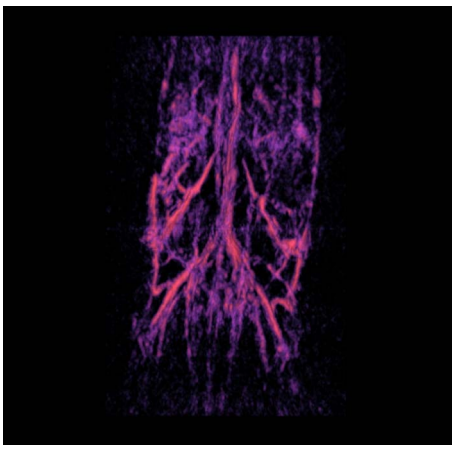

Video 4 This video corresponds to Fig. 8, showing an optoacoustic volume of a nude mouse illuminated at 1064 nm at optical fluence of 1 mJ/cm^2, which displays the mouse body vasculature including descending inferior vena cava and its bifurcation into the external and internal femoral veins and the three tail veins. Additionally, there is a partial view of the left and right kidney vasculature (QuickTime, 758 KB). [URL: http://dx.doi.org/10.1117/1.3259361.4].

out of the fiber bundles led to a reduced fluence at the upper and lower parts of the mouse body and led to less optoacoustic signal generated. The reduced signal from these areas did not exceed the threshold value set in the image reconstruction, making these parts of the body faint or invisible. In some experiments, we were able to visualize the heart and lungs of a mouse. However, heterogeneous and air-containing tissue structures such as lungs generate significant noise and negative pressure values in the voxels at the tissue-air interfaces. These voxels were later removed in the image processing to clear up the overall image. Visualization of the heart and malignant tumors will enable important applications of our system in preclinical research. This will be the subject of our future research and development.

The current ~0.5-mm resolution limits the detection of finer structures. On the other hand, in case of sufficient contrast, smaller vasculature (such as ovarian vessels) and other small tissue structures can still be visualized with our system. However, the true size of these objects is smaller than they appear. For example, the descending aorta measures ~1.5 mm in the mouse, but measures 2 mm in the reconstructed volume.

Illumination with four equally spaced fiber bundles might provide even more homogenous optical illumination. However, this configuration requires modification of the present light delivery system to avoid optoacoustic signals caused by direct illumination of the transducer array and optical backreflection from the skin of the mouse onto the transducers. Therefore, in the presented system design, illumination with two optical beams orthogonal to the array of transducers provided the best compromise between uniform illumination and reduction of unwanted optoacoustic signals.

The time currently required to complete the 150 data acquisitions of 2.4-deg steps for the full 360-deg scan is 8 min using averaging over 32 laser pulses. Modification of the stepper motor and its electronic controller (driver) should reduce external noise acquired by the system electronics, which in turn will enable us to speed up data acquisition to perform functional studies, such as monitoring hypoxia in live mice. Ultimately, with the proper attention to noise reduction, the time of a full scan can be decreased to 15 s using a 10-Hz repetition rate of laser pulses. The most frequently used signal processing method was the wavelet filtering, and the most frequently used image processing method was the gradient opacity mapping. Currently, the time for 3-D image reconstruction using standard computer processing units (CPUs) is several hours and rapidly increases with increasing image resolution. Transfer of the tomographic image reconstruction to a graphical processing unit (GPU) may reduce the time to a few minutes. Note also that while our tomography algorithm compensated for the higher transducer density at the poles of the spherical volume being reconstructed, the transducers were considered dimensionless. Incorporation of the spatial impulse response of the optoacoustic transducers with real physical dimensions and more sophisticated signal and image processing methods will improve contrast and resolution of the reconstructed images.

5 Conclusion

A 3-D whole-mouse-body optoacoustic tomography system was developed for applications in preclinical research. The average image resolution through the field of view of $40\times40\times60$ mm was ~0.5 mm. Optoacoustic images were obtained using 755- and 1064-nm laser wavelengths. The 3-D tomography was obtained using complete sets of optoacoustic signal data in the spherical coordinates and clearly showed blood-rich internal organs such as liver, spleen, and kidneys as well as large and small vasculature. Future work will concentrate on improving the speed of data acquisition and improving image contrast and resolution using modern tools of signal and image processing.

Acknowledgments

This work was supported in part by grants from the National Cancer Institute (R44CA110137, R44CA128196) and Seno Medical Instruments, Inc. (San Antonio, Texas). We thank the technical staff of Fairway Medical Technologies for their contributions to engineering and assembly of the system components.

References

1. H. D. Liang and M. J. K. Blomley, "The role of ultrasound in molecular imaging," *Br. J. Radiol.* **76**, 140–150 (2003).
2. L. A. Wirtzfeld, G. Wu, M. Bygrave, Y. Yamasaki, H. Sakai, M. Moussa, J. I. Izawa, D. B. Downey, N. M. Greenberg, A. Fenster, J. W. Xuan, and J. C. Lacefield, "A new three-dimensional ultrasound microimaging technology for preclinical studies using a transgenic prostate cancer mouse model," *Cancer Res.* **65**(14), 6337–6345 (2005).
3. C. T. Badea, M. Drangova, D. W. Holdsworth, and G. A. Johnson, "*In vivo* small-animal imaging using micro-CT and digital subtraction angiography," *Phys. Med. Biol.* **53**(19), R319–350 (2008).
4. R. G. Pautler and S. E. Fraser, "The year(s) of the contrast agent—micro-MRI in the new millennium," *Curr. Opin. Immunol.* **15**(4), 385–392 (2003).
5. P. Vaska, D. J. Rubins, D. L. Alexoff, and W. K. Schiffer, "Quantitative imaging with the micro-PET small-animal PET tomograph," *Int. Rev. Neurobiol.* **73**, 191–218 (2006).
6. R. T. Sadikot and T. S. Blackwell, "Bioluminescence imaging," *Proc. Am. Thorac. Soc.* **2**(6), 537–540 (2005).
7. V. Ntziachristos, C. Bremer, and R. Weissleder, "Fluorescence imag-

ing with near-infrared light: new technological advances that enable *in vivo* molecular imaging," *Eur. Radiol.* **13**(1), 195–208 (2003).
8. A. H. Hielscher, "Optical tomographic imaging of small animals," *Curr. Opin. Biotechnol.* **16**(1), 79–88 (2005).
9. U. Mahmood, C. H. Tung, A. J. Bogdanov, and R. Weissleder, "Near-infrared optical imaging of protease activity for tumor detection," *Radiology* **213**(3), 866–870 (1999).
10. A. A. Oraevsky and A. A. Karabutov, "Optoacoustic tomography," in *Biomedical Photonics Handbook*, T. Vo-Dinh, Ed., pp. 34/31–34/34, CRC Press, Boca Raton, London, New York, Washington, DC (2003).
11. H. P. Brecht, D. S. Rough, Y. Y. Petrov, I. Y. Petrova, D. J. Deyo, and R. O. Esenaliev, "Accurate, noninvasive measurement of total hemoglobin concentration with optoacoustic technique," in *Conf. Proc. IEEE Eng. Med. Biol. Soc.* Vol. **1**, pp. 375–376 (2004).
12. A. A. Oraevsky, E. A. Savateeva, S. V. Solomatin, A. A. Karabutov, V. G. Andreev, Z. Gatalica, T. Khamapirad, and P. M. Henrichs, "Optoacoustic imaging of blood for visualization and diagnostics of breast cancer," *Proc. SPIE* **4618**, 81–94 (2002).
13. R. G. M. Kolkman, E. Hondebrink, W. Steenbergen, and F. F. M. de Mul, "*In vivo* photoacoustic imaging of blood vessels using an extreme-narrow aperture sensor," *IEEE J. Sel. Top. Quantum Electron.* **9**(2), 343–346 (2003).
14. K. Maslov, G. Stoica, and L. V. H. Wang, "*In vivo* dark-field reflection-mode photoacoustic microscopy," *Opt. Lett.* **30**(6), 625–627 (2005).
15. X. D. Wang, Y. J. Pang, G. Ku, G. Stoica, and L. H. V. Wang, "Three-dimensional laser-induced photoacoustic tomography of mouse brain with the skin and skull intact," *Opt. Lett.* **28**(19), 1739–1741 (2003).
16. E. Z. Zhang, J. G. Laufer, R. B. Pedley, and P. C. Beard, "*In vivo* high-resolution 3D photoacoustic imaging of superficial vascular anatomy," *Phys. Med. Biol.* **54**(4), 1035–1046 (2009).
17. S. A. Ermilov, T. Khamapirad, A. Conjusteau, M. H. Leonard, R. Lacewell, K. Mehta, T. Miller, and A. A. Oraevsky, "Laser optoacoustic imaging system for detection of breast cancer," *J. Biomed. Opt.* **14**(2), 024007 (2009).
18. S. Manohar, A. Kharine, J. C. G. van Hespen, W. Steenbergen, and T. G. van Leeuwen, "The Twente photoacoustic mammoscope: system overview and performance," *Phys. Med. Biol.* **50**(11), 2543–2557 (2005).
19. J. T. Oh, M. L. Li, H. F. Zhang, K. Maslov, G. Stoica, and L. H. V. Wang, "Three-dimensional imaging of skin melanoma *in vivo* by dual-wavelength photoacoustic microscopy," *J. Biomed. Opt.* **11**(3), 034032 (2006).
20. G. Ku, X. D. Wang, X. Y. Xie, G. Stoica, and L. H. V. Wang, "Imaging of tumor angiogenesis in rat brains *in vivo* by photoacoustic tomography," *Appl. Opt.* **44**(5), 770–775 (2005).
21. R. G. M. T. Kolkman, K. K. Thumma, G. A. ten Brinke, R. I. Siphanto, H. van Neck, W. Steenbergen, and T. G. von Leeuwen, "Photoacoustic imaging of tumor aniogenesis," *Proc. SPIE* **6856**, 685602 (2008).
22. G. F. Lungu, M. L. Li, X. Y. Xie, L. H. V. Wang, and G. Stoica, "*In vivo* imaging and characterization of hypoxia-induced neovascularization and tumor invasion," *Int. J. Oncol.* **30**(1), 45–54 (2007).
23. L. Z. Xiang, D. Xing, H. M. Gu, D. W. Yang, S. H. Yang, L. M. Zeng, and W. R. Chen, "Real-time optoacoustic monitoring of vascular damage during photodynamic therapy treatment of tumor," *J. Biomed. Opt.* **12**(1), 014001 (2007).
24. R. A. Kruger, W. L. Kiser Jr., D. R. Reinecke, and G. A. Kruger, "Thermoacoustic computed tomography using a conventional linear transducer array," *Med. Phys.* **30**(5), 856–860 (2003).
25. V. G. Andreev, A. A. Karabutov, S. V. Solomatin, E. A. Savateeva, L. V. Aleynikov, Y. V. Zhulina, D. R. Fleming, and A. A. Oraevsky, "Optoacoustic tomography of breast cancer with arc-array transducer," *Proc. SPIE* **3916**, 36–47 (2000).
26. R. A. Kruger, W. L. Kiser, D. R. Reinecke, G. A. Kruger, and K. D. Miller, "Thermoacoustic molecular imaging of small animals," *Mol. Imaging* **2**(2), 113–123 (2003).
27. X. Wang, X. Xie, G. Ku, L. V. Wang, and G. Stoica, "Noninvasive imaging of hemoglobin concentration and oxygenation in the rat brain using high-resolution photoacoustic tomography," *J. Biomed. Opt.* **11**(2), 024015 (2006).
28. A. Oraevsky, "Gold and silver nanoparticles as contrast agents for optoacoustic imaging," in *Photoacoustic Imaging and Spectroscopy*, L. Wang, Ed., Taylor and Francis Group, New York (2009).
29. M. Eghtedari, A. Oraevsky, J. A. Copland, N. Kotov, A. Conjusteau, and M. Motamedi, "High sensitivity of *in vivo* detection of gold nanorods using a laser optoacoustic imaging system," *Nano Lett.* **7**(7), 1914–1918 (2007).
30. Y. Wang, X. Xie, X. Wang, G. Ku, K. L. Gill, D. P. O'Neal, G. Stoica, and L. V. Wang, "Photoacoustic tomography of a nanoshell contrast agent in the *in vivo* rat brain," *Nano Lett.* **4**(9), 1689–1692 (2004).
31. X. Yang, S. E. Skrabalak, Z. Y. Li, Y. Xia, and L. V. Wang, "Photoacoustic tomography of a rat cerebral cortex *in vivo* with AU nanocages as an optical contrast agent," *Nano Lett.* **7**(12), 3798–3802 (2007).
32. H.-P. Brecht, R. Su, M. Fronheiser, S. A. Ermilov, A. Conjusteau, and A. A. Oraevsky, "Optoacoustic 3D whole body tomography: experiments in nude mice," *Proc. SPIE* **7177**, 71770E (2009).
33. I. Patrikeev and A. A. Oraevsky, "Multiresolution wavelet reconstruction method for optoacoustic tomography," *Proc. SPIE* **4960**, 99–105 (2003).
34. S. A. Ermilov, A. Stein, A. Conjusteau, R. Gharieb, R. Lacewell, T. Miller, S. Thompson, P. Otto, B. McCorvey, T. Khamapirad, M. H. Leonard, and A. A. Oraevsky, "Detection and noninvasive diagnostics of breast cancer with two-color laser optoacoustic imaging system," *Proc. SPIE* **6437**, 6437031–64370310 (2007).
35. A. Oraevsky, "Optoacoustic tomography of the breast," in *Photoacoustic Imaging and Spectroscopy*, L. Wang, Ed., Taylor and Francis Group, New York (2009).
36. T. Iwaki, *A Color Atlas of Sectional Anatomy of the Mouse*, Adthree Publishing Co., Ltd., Tokyo (2001).